Engineering Structures 284 (2023) 115992

Contents lists available at ScienceDirect

Engineering Structures

journal homepage: www.elsevier.com/locate/engstruct

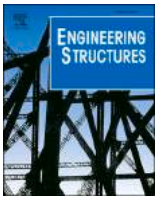

Flexural strengthening of reinforced concrete beams using hybrid fibre reinforced engineered cementitious composite

M. Qasim [a], C.K. Lee [a], Y.X. Zhang [b,*]

[a] School of Engineering and Information Technology, University of New South Wales, Canberra, 2600 NSW, Australia
[b] School of Engineering, Design and Built Environment, Western Sydney University, Penrith, NSW 2751, Australia

ARTICLE INFO

Keywords:
Flexural strengthening
Hybrid fibre reinforced engineered cementitious composite
Reinforced concrete beams
Numerical modelling
Interfacial bond-slip

ABSTRACT

In this study, flexural strengthening of reinforced concrete (RC) beams using steel and polyvinyl-alcohol hybrid fibre reinforced engineered cementitious composite (SPH-ECC) with embedded steel reinforcement bars is proposed. The effectiveness of the strengthening was investigated by experimental and numerical studies. The flexural behaviours of one unstrengthened 3500 mm long, 200 mm wide, and 325 mm deep RC beam and three RC beams strengthened with different configurations of 50 mm thick SPH-ECC layer(s) were studied by conducting four-point bending tests. Detailed flexural behaviours in terms of peak load, failure mode, load-deflection curve, cracking patterns, interfacial bond-slip, strain distribution and ductility of the tested beams were studied and compared. Experimental results showed that both the flexural strength of strengthened beams, which were in the range of 125% to 210% of the unstrengthened control beam, and the interfacial bond-slip behaviours between concrete and SPH-ECC was highly depended to the strengthening configuration used. Crack width control ability of the beams was also improved by using SPH-ECC. A finite element (FE) procedure using surface-to-surface cohesive model was also developed to model the flexural behaviours of the strengthened beams. Comparison with experimental results demonstrated that the proposed FE model could accurately predict the flexural behaviours including interfacial bond-slip between the SPH-ECC layers and the RC beam part of the strengthened beams.

1. Introduction

Demand for strengthening reinforced concrete (RC) structures is increasing worldwide due to the increasing deterioration of many existing RC structures [1–3]. Many techniques and methods have been proposed and used for strengthening the flexural strength of RC beam. These include RC jacketing [4–7], steel fibre reinforced concrete (SFRC) jacketing [8–11], use of externally bonded steel plates [12–15] and fibre reinforced polymers (FRP) strips [16–18]. However, the low interfacial bond strength of RC jacket with concrete [19] and its brittle nature make it unsuitable for ductility improvement [20]. While SFRC jacketing had shown a good interfacial bond strength with concrete, its ductility was also low [21]. For FRP strips and steel plates, they are prone to premature failure due to delamination from the concrete surface. Moreover, FRP strips generally have poor fire resistance and may generate harmful fumes in fire [22].

In order to strengthen RC structures effectively, it is therefore essential to employ a material with desired ductility which can also provide considerable strength without deterioration under elevated temperatures. Steel and polyvinyl-alcohol hybrid fibre reinforced engineered cementitious composite (SPH-ECC), which is a special type of engineered cementitious composite (ECC), is a promising candidate due to its high ductility under both compression and tension and it has reasonably good fire resistance. Mono-fibre reinforced ECC such as polyvinyl-alcohol fibre reinforced ECC (PVA-ECC) has been used to strengthen RC structures [20,23–27]. Krishnaraja and Kandasamy [28] found that both SPH-ECC and PVA-ECC have similar interfacial bond strengths with normal concrete. However, PVA-ECC has lower ultimate strength and low fire resistance [29]. Towards this end, hybrid fibre reinforced ECC such as SPH-ECC could provide a higher ultimate strength [30,31], better fire resistance [32] as well as better protection for steel reinforcement bars against corrosion when compared with mono-fibre reinforced ECC [33]. However, currently very few detailed studies have been conducted to evaluate the effectiveness of using hybrid fibre reinforced ECC for strengthening of RC structures.

Recently, Tinoco and Silva [34] studied the strengthening effects of

* Corresponding author at: School of Engineering and Information Technology, University of New South Wales, Canberra, 2600 NSW, Australia.
E-mail address: sarah.zhang@westernsydney.edu.au (Y.X. Zhang).

https://doi.org/10.1016/j.engstruct.2023.115992

Available online 23 March 2023

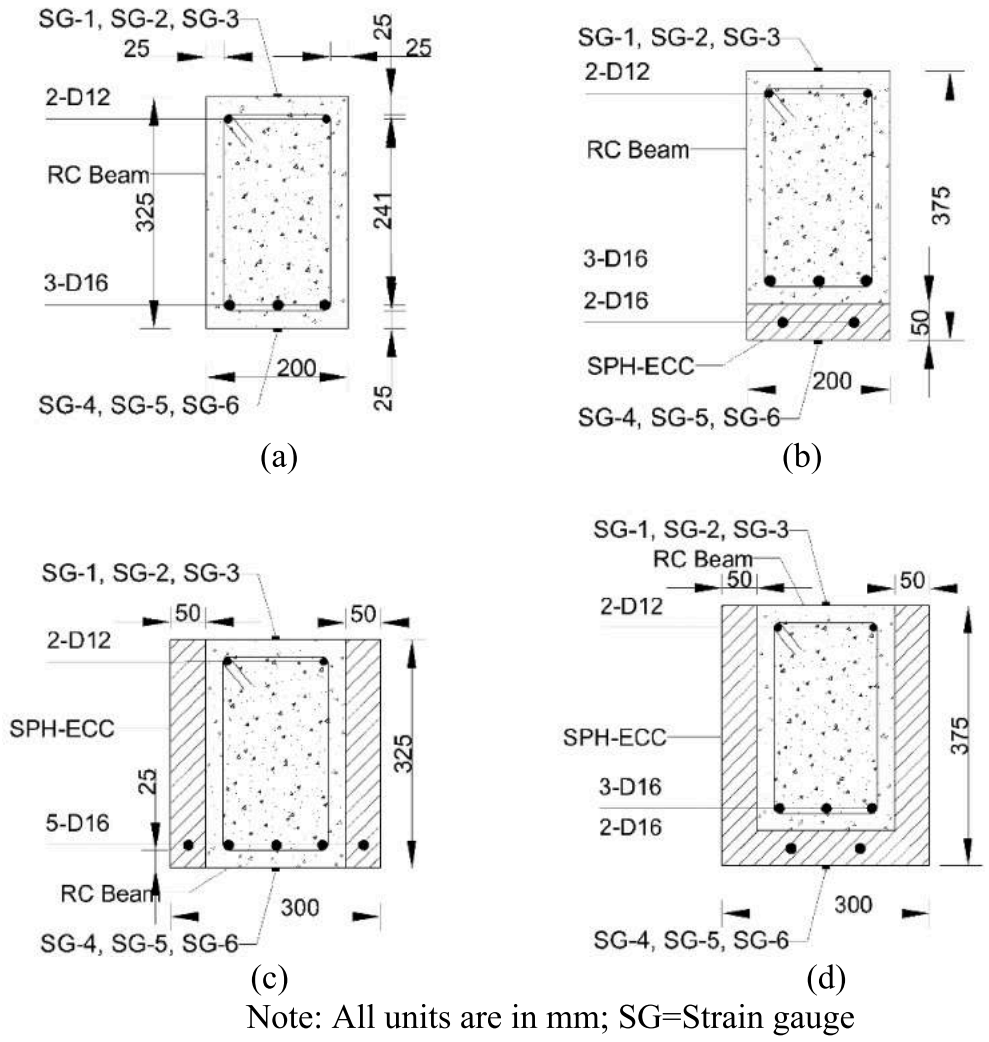

Fig. 1. Cross-sectional details of beams. (a) CB, (b) SB-1, (c) SB-2, (d) SB-3.

SPH-ECC without any embedded reinforcement bar by conducting flexural tests on some scaled RC beams which were 1200 mm long, 120 mm wide and 150 mm deep. The interfacial surface between SPH-ECC and concrete was roughened using 20 mm wide and 5 mm deep grooves with 60 mm spacing which resulted in no interfacial debonding during flexural tests. Moreover, test results [34] showed that ductility during the post-peak region was significantly reduced. Based on the study of Lu and Leung [35], it was argued by Tinoco and Silva [34] that the flexural ductility of full-scale strengthened RC beams with SPH-ECC would be different to their study. It was also observed that the use of SPH-ECC without any embedded reinforcement bar could only achieve an insignificant increase in flexural strength when compared with the unstrengthened beams [34]. Therefore, embedding reinforcement bars within the SPH-ECC layer might have a high potential to enhance the flexural strength of RC beams significantly and the effectiveness of such strengthening approach should be evaluated.

This study was conducted with an objective to investigate the flexural performance of full-scale strengthened RC beams, using SPH-ECC layer(s) with embedded reinforcement bars, in terms of peak load, failure mode, load-midspan deflection curve, cracking pattern, interfacial bond-slip, strain distribution and ductility. As-cast interfacial surface without any additional surface treatment was used between the SPH-ECC layer(s) and the RC beam part. Normal strength steel (NSS) reinforcement bars were embedded inside the SPH-ECC layer(s). One unstrengthened 3500 mm long, 200 mm wide and 325 mm deep RC beam and three strengthened RC beams with 50 mm thick SPH-ECC

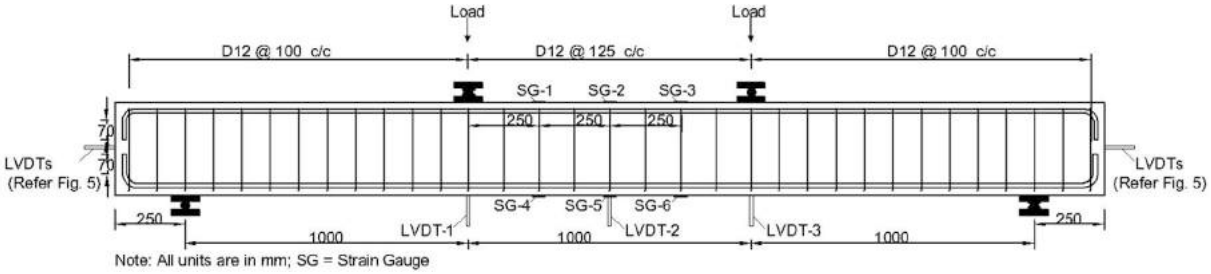

Fig. 2. Longitudinal section of RC beam, instrumentation, loading and support details.

Fig. 3. Formwork used for the beam fabrication. (a) CB, (b) SB-1, (c) SB-2, (d) SB-3.

layer(s) applied in different geometric configurations were tested to compare their flexural behaviours. In addition to the experimental study, in order to obtain a deeper insight on the flexural behaviours of the strengthened beams including the interfacial bond behaviour between the SPH-ECC layer(s) and the RC beam part which is the weakest link of many strengthening systems [36–39], an FE procedure was also developed by using the general purpose FE program ABAQUS [40]. The proposed model used a surface-to-surface cohesive model to describe the interfacial bond behaviour between the SPH-ECC and concrete surfaces. The experimental results obtained were then employed to validate the proposed model.

2. Experimental program

2.1. Specimen configurations and preparation

In this study, one unstrengthened RC control beam (CB) and three strengthened RC beams (SB-1, SB-2 and SB-3) with different configurations of the SPH-ECC layer(s) and embedded NSS reinforcement bars were tested under four-point bending loading. The cross-sectional configurations of these beams and their reinforcement bars details are shown in Fig. 1. The longitudinal section of the CB as well as the loading and support conditions are shown in Fig. 2. The CB (Fig. 1a) had nominal dimensions of 200 mm (width) × 325 mm (height) × 3500 mm (total length). The CB was designed to be under-reinforced with three 16 mm diameter (D16) reinforcement bars placed at the bottom and two 12 mm diameter (D12) reinforcement bars used as hanger bars at top. In order to provide sufficient shear resistance, D12 stirrups were used with 100 mm and 125 mm centre to centre spacing in the shear and flexural spans, respectively. For the strengthened beams, three different configurations for applying the SPH-ECC layers were adopted. For SB-1 (Fig. 1b), only one SPH-ECC layer was applied at the bottom of the RC beam part with two D16 reinforcement bars. For SB-2 (Fig. 1c), two SPH-ECC layers were applied at the two sides of the RC beam part and one D16 reinforcement bar was used at each side. For SB-3 (Fig. 1d), SPH-ECC layers were applied at both sides and the bottom of the RC beam part to form a U-shape encasement with two D16 reinforcement bars placed at the bottom. These layers were applied under the as-cast condition without any construction joint nor roughening of the concrete surface. It should be noted that at each end of all the main reinforcement bars in RC beams and SPH-ECC layers, 90° bend with 70 mm extended length was provided to achieve a perfect interfacial bond between concrete/SPH-ECC and reinforcement bars. Furthermore, as all beams tested were based on full-scale dimensions using in practical applications, each test actually expensive (in terms of materials, labour cost and time) to conduct. Hence, only one beam for each configuration was tested due to limitations on time and resources available.

The formworks used for the CB, SB-1, SB-2 and SB-3 beams were shown in Fig. 3. For the CB, the reinforcement cage was fabricated and then placed in the formwork (Fig. 3a) before concrete was poured. The concrete beams were demoulded after 24 h and cured for an additional ***55*** days at a constant temperature of 23 °C under 100% relative humidity inside a fog room with automatic humidity and temperature controls before testing. For the strengthened beams, their RC beam parts were first cast in an exact way as the CB. At the age of *28* days, the RC beam parts were moved into the formworks shown in Fig. 3b, 3c and 3d, respectively. 50 mm thick SPH-ECC layer(s) were then applied on the as-cast surface of RC beams according to the configurations shown in Fig. 1. It should be noted that for SB-1 and SB-3, the RC beam parts were first rotated up-side- down before reinforcement bars and SPH-ECC layer(s) were casted. For SB-2, no rotation was required as reinforcement bars and SPH-ECC layers could be easily placed on both sides of the beam. The strengthened beams were then demoulded after 24 h and cured for an additional *27* days before testing. Thus, the CB and the RC beam parts of the strengthened beams had been cured for 56 days when they were tested. It should be noted that due to the volume limitation of the

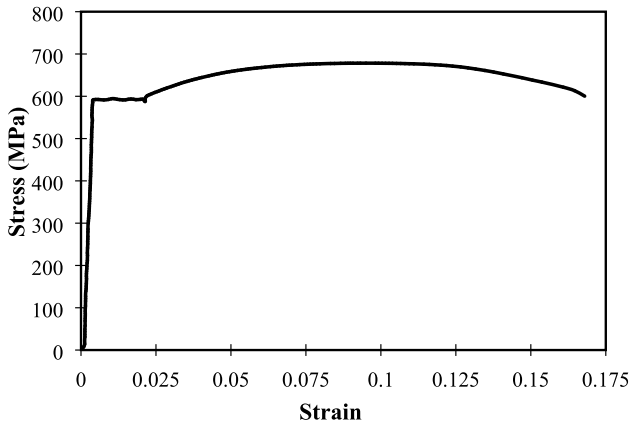

Fig. 4. Typical uniaxial stress-strain curve of steel reinforcement bars.

Table 1
Concrete and SPH-ECC mix designs.

Material	Concrete		SPH-ECC	
	/c	Kg/m^3	/c	Kg/m^3
Cement	1	320	1	571
Fly ash	–	–	1.2	456
Sand	2.5	800	0.8	685
Coarse aggregate	4	1280	–	–
Water	0.6	192	0.6	343
HRWR	–	–	0.013	7.4
PVA fibre (Volume Percentage)	–	–	1.47%	19.11
Steel fibre (Volume Percentage)	–	–	0.73%	56.94

Table 2
Mechanical properties of concrete and SPH-ECC.

Mechanical Property	Unit	Concrete	SPH-ECC		
			SB-1	**SB-2**	**SB-3**
Compressive strength	MPa	31.9	66.0	70.6	78.5
Elastic modulus	GPa	28.06	19.7	20.5	20.1
Uniaxial tensile strength for SPH-ECC	MPa	–	4.62	6.14	6.98
Splitting tensile strength for concrete	MPa	2.99	–	–	–
Tensile strain for SPH-ECC	%	–	0.47	0.58	0.64

concrete mixer and to reuse formwork materials to minimum waste, castings of the four beams were not started on the same day. The CB and the RC beam part of SB-3 was cast at the same day. For SB-1 and SB-2, their fabrications were started four and five weeks later, respectively. Thus, three separate concrete and SPH-ECC mixes were prepared for the strengthened beams. The material properties of the concrete and SPH-ECC were determined at the test day.

2.2. Material properties

The mechanical properties of D12 and D16 reinforcement bars were obtained through uniaxial tensile test according to ASTM A370 [41]. For both types of reinforcement bars, a yield strength of $f_y = 590$ MPa and an ultimate tensile strength of $f_u = 680$ MPa were recorded as shown in Fig. 4. All reinforcement bars had the same elastic modulus of 190 GPa with a yield strain of 0.31%.

Based on a preliminary estimation to match the loading capacity of the test rig and to ensure that all beams are under-reinforced, concrete mix design with characteristic compressive strength of 30 MPa was selected. The mix design for the concrete was given in Table 1. Coarse aggregate with maximum size of 14 mm and general-purpose cement

Table 3
Geometric and mechanical properties of PVA fibres and steel fibres.

Type of fibre	Diameter (μm)	Length (mm)	Tensile strength (MPa)	Young's modulus (GPa)	Specific gravity
PVA Fibre	39	12	1620	42.8	1.3
Steel Fibre	200	13	2750	210	7.85

was used in concrete. From standard cylinder tests, it was found that the mechanical properties of all three concrete mixes were highly consistent with an average compressive strength of 31.9 MPa (Table 2). The average indirect tensile strength which was obtained through test as per ASTM C496 was 2.99 MPa. The average elastic modulus of concrete was 28.06 GPa.

For SPH-ECC, based on a preliminary estimation, a target minimum compressive strength of 60 MPa was selected. The mix design of PVA-ECC proposed by Meng et al. [42] was employed as a base to develop the mix design of SPH-ECC while the mixing procedure described by Khan et al. [43] was adopted to produce the SPH-ECC. The ingredients used were comprised of general-purpose cement, ASTM class F fly ash, local dune sand with maximum particle size of 300 μm, water, PVA fibre and steel fibre. The geometric and mechanical properties of the PVA and steel fibres used are shown in Table 3. ADVA 650 [44] high range water reducer which complies with AS 1478.1 [45] was used to maintain a reasonable flowability. A total fibre volume percentage of 2.2% was used. Mix design for the SPH-ECC is summarized in Table 1. Note that the volume fraction of steel (0.73%) and PVA (1.47%) fibres were selected to achieve the desired strength with good ductility. The compressive strength and elastic modulus of SPH-ECC were obtained by standard cylinder test [42] while direct tensile test using dog-bone specimens [42] was employed to obtain the uniaxial tensile strength. The averaged values of mechanical properties of the SPH-ECC used for the three strengthened beams are shown in Table 2. It can be seen from Table 2 that their compressive strengths were all higher than the target value of 60 MPa.

2.3. Test setup and procedures

All four beams were tested under a four-point bending configuration so that the length of both the pure bending span and the shear span is 1000 mm (Fig. 2). Vertical load was applied under displacement control at a rate of 1 mm/min [46] until obvious concrete crushing and spalling was observed at the top surface of the beams. Three linear variable differential transformers (LVDTs) were installed in the pure bending span to measure the deflections at the midspan of beam and the loading points. For the strengthened beams, additional LVDTs were attached at the support ends (Fig. 5) to capture any interfacial bond slip between the SPH-ECC layers and the RC beam part. From Fig. 5, it can be seen that the LVDT arrangement for each beam was designed based on the configuration of the strengthened scheme. In order to measure the strains at the top and bottom surfaces of the beams, strain gauges were installed as shown in Fig. 1 and Fig. 2. Digital image correlation (DIC) technique was used to capture the damage and crack propagation history by using three high-resolution DSLR cameras which covered the entire beam as shown in Fig. 6.

3. Experimental results

3.1. Failure modes and load-midspan deformation curves

Fig. 7 summarizes the load-midspan deflection curves of all beams. The failure modes of these beams are shown in Fig. 8. From the test results and Fig. 7, it was found that the load-midspan deflection curves

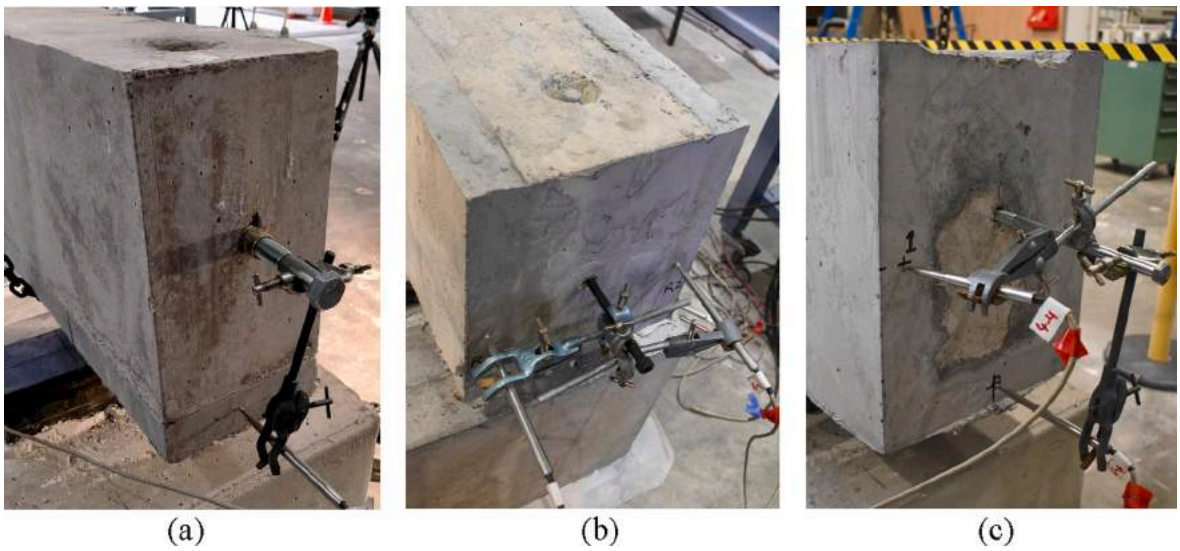

Fig. 5. LVDTs set up at support ends for interfacial bond-slip measurement. (a) SB-1, (b) SB-2, (c) SB-3 beams.

Fig. 6. DSLR cameras setup for DIC analysis.

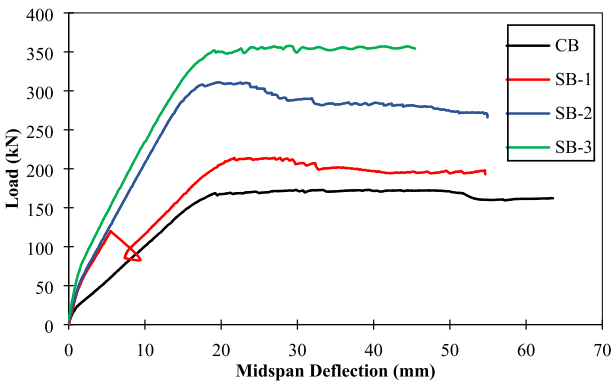

Fig. 7. Load-midspan deflection curves of tested beams.

of CB, SB-2 and SB-3 generally showed three distinctive phases namely, (1) the uncracked phase, (2) the crack forming/propagation phase and (3) the final failure phase. During the first uncracked phase, the load increased linearly with the midspan-deflection. The cracking phase was then started after some micro-cracks were formed so that the slope of the load-midspan deflection curve was decreased slightly. The curves then continued with an almost constant slope until the yielding of longitudinal reinforcement bars. At the end of the cracking phase, the slope of the curve decreased to almost zero when the final failure phase started. In the final phase, the mid-span deflection increased without further increase of the sustained load until the beam failed due to concrete crushing at the top surface of the pure bending span for the CB, SB-2 and SB-3. (Fig. 8a, c and d). For SB-1, while the deflection curve also generally showed these three distinctive phases, premature interfacial debonding between the RC beam part and the ECC layer was occurred shortly after the cracking phase started. This resulted in a sudden drop of the sustained load and the slope of the deflection curve.

(a)

(b)

(c)

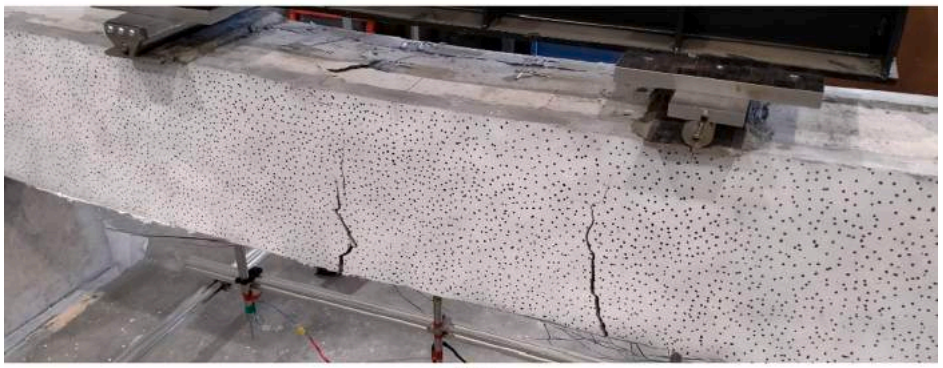

(d)

Fig. 8. Failure modes of tested beams. (a) CB, (b) SB-1, (c) SB-2, (d) SB-3.

3.1.1. The CB beam

For the CB, yielding of the reinforcement bars started before the load of 130 kN. It reached a peak load of 168.5 kN at a corresponding mid-span deflection of 19.2 mm. After that the load remained almost constant until failure in form of concrete crushing at a midspan-deflection of 52 mm. At the end of the test, extensive cracking was observed in the pure bending span as shown in Fig. 8a.

3.1.2. The SB-1 beam

For SB-1, shortly after the cracking phase started, interfacial debonding between the SPH-ECC layer and RC beam part occurred at a midspan deflection of 5.26 mm (Fig. 7). The interfacial debonding

Fig. 9. Interfacial bond-slip at the L.H.S. support end of SB-1 at beam failure.

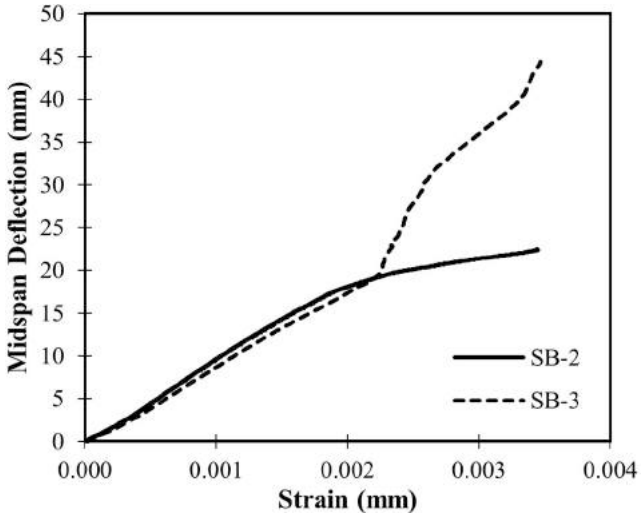

Fig. 10. Midspan-deflection vs compressive strain obtained by SG-2 at the top mid-span concrete surface for the SB-2 and SB-3 beams.

mainly occurred at the left hand side (LHS) shear span of the beam with a clear bond slip observed at the LHS support end (Fig. 9). Such debonding was similar to the results obtained by Wu and Li [46] in which PVA-ECC layer was applied at the RC beam soffit with embedded strips of carbon fibre reinforced polymer as reinforcement layer. On the other hand, Tinoco and Silva [34] observed no debonding when the tested RC beams were strengthened in similar configuration to SB-1 by SPH-ECC but *without* any embedded reinforcement bars. Furthermore, more detailed analysis of the load-deflection curve showed that the stiffness of SB-1 before debonding (15.22×10^3 kN/m) was much higher than that of CB (8.88×10^3 kN/m). Thus, it can be concluded that interfacial debonding in SB-1 could be due to the increased stiffness of SPH-ECC layer caused by the embedded reinforcement bars and the relatively small contact area available to resist the interfacial stress developed. After debonding, the stiffness was decreased to 9.89×10^3 kN/m which was only slightly higher than that of the CB as the SPH-ECC layer was bent independently and only made a small contribution to the beam stiffness. Immediately after the debonding, tensile cracks were observed within the RC beam part of SB-1. At the end of the test, the failure mode of the RC beam part was found to be very similar to that of the CB with little damage observed in the SPH-ECC layer. The maximum recorded load was 213.4 kN which was only 26.6% higher than that of the CB.

3.1.3. The SB-2 beam

For SB-2, the uncrack phase ended when the loading reached approximately 55 kN. After that, the crack phase started with multiple micro-cracks initiated in the SPH-ECC the layer within the pure bending span. These cracks were widened and became very obvious near the end of the cracking phase when the applied load reached 270 kN. Between 270 kN and 310 kN, yielding of reinforcement bars in SPH-ECC led to gradual stiffness reduction. This eventually accelerated the tensile strain softening phenomenon in the SPH-ECC layers and resulted in crack localization so that the beam's capacity remained almost constant when the midspan deflection was increased from 17.5 mm to 22.4 mm of (Fig. 7). Immediately after that, the concrete compressive strains at the midspan top surface (recorded by strain gauge SG-2, Fig. 2) reached the concrete crushing strain of 0.33% (Fig. 10). This resulted in a gradual drop of the load capacity. The peak load recorded was 310kN which is 184% of the CB. No interfacial bond slip between SPH-ECC layer and the RC beam part was observed before the concrete crushing. However, immediately after the concrete crushing, interfacial debonding was observed. However, no sudden load drop due to such interfacial debonding was observed.

3.1.4. The SB-3 beam

For SB-3 with SPH-ECC layers formed a U-shape encasement around the RC beam part, it showed a peak load of 354 kN which was 210% of the CB and was the highest among all the strengthened beams. Uncrack phase for the SB-3 ended when the loading was approximately 75kN while the cracking phase continued up to a loading of about 320kN. Multiple observable cracks then appeared within SPH-ECC bottom layer in the pure bending span and the peak load was achieved when the midspan deflection was about 20 mm. The load then remained almost constant with substantial crack localization until the beam failed at a midspan deflection of 46 mm. When failure occurred, strain at the midspan top surface was found to reach the concrete crushing limit of 0.33% (Fig. 10). Unlike SB-1 and SB-2, no substantial interfacial debonding was observed even after concrete crushing occurred. This could be attributed to the U-shape encasement of SB-3 which gave the largest interfacial area between the SPH-ECC layers and the RC beam part among the three strengthened beams.

3.2. Interfacial bond behaviour

The interfacial bond between strengthening layer and RC beam part is one of the most critical factors affecting the performance of a strengthening system [36–39]. In case of insufficient interfacial bond strength, premature failure may occur due to debonding. Therefore, for the strengthened beams, the interfacial bond-slip was monitored continuously between the SPH-ECC layer(s) and RC beam parts during the tests. The relative displacements of SPH-ECC layer(s) with respect to the RC beam part was recorded using LVDTs shown in Fig. 5. Interfacial bond-slip values recorded at two support ends for the strengthened beams are then plotted against the midspan deflection in Fig. 11 together with the load-midspan deflection curves. For SB-1, from Fig. 11a, when the applied load was approximately 119 kN, a jump of interfacial bond-slip from almost zero to 0.9 mm occurred in the LHS shear span together with a sudden drop of the applied load. After that, LHS bond-slip was increased steadily until failure while the right hand side (RHS) bond-slip remained almost zero.

For SB-2 (Fig. 11b) and SB-3 (Fig. 11c), it should be noted that the "front side" SPH-ECC layer refers to the layer which was facing the DSLR

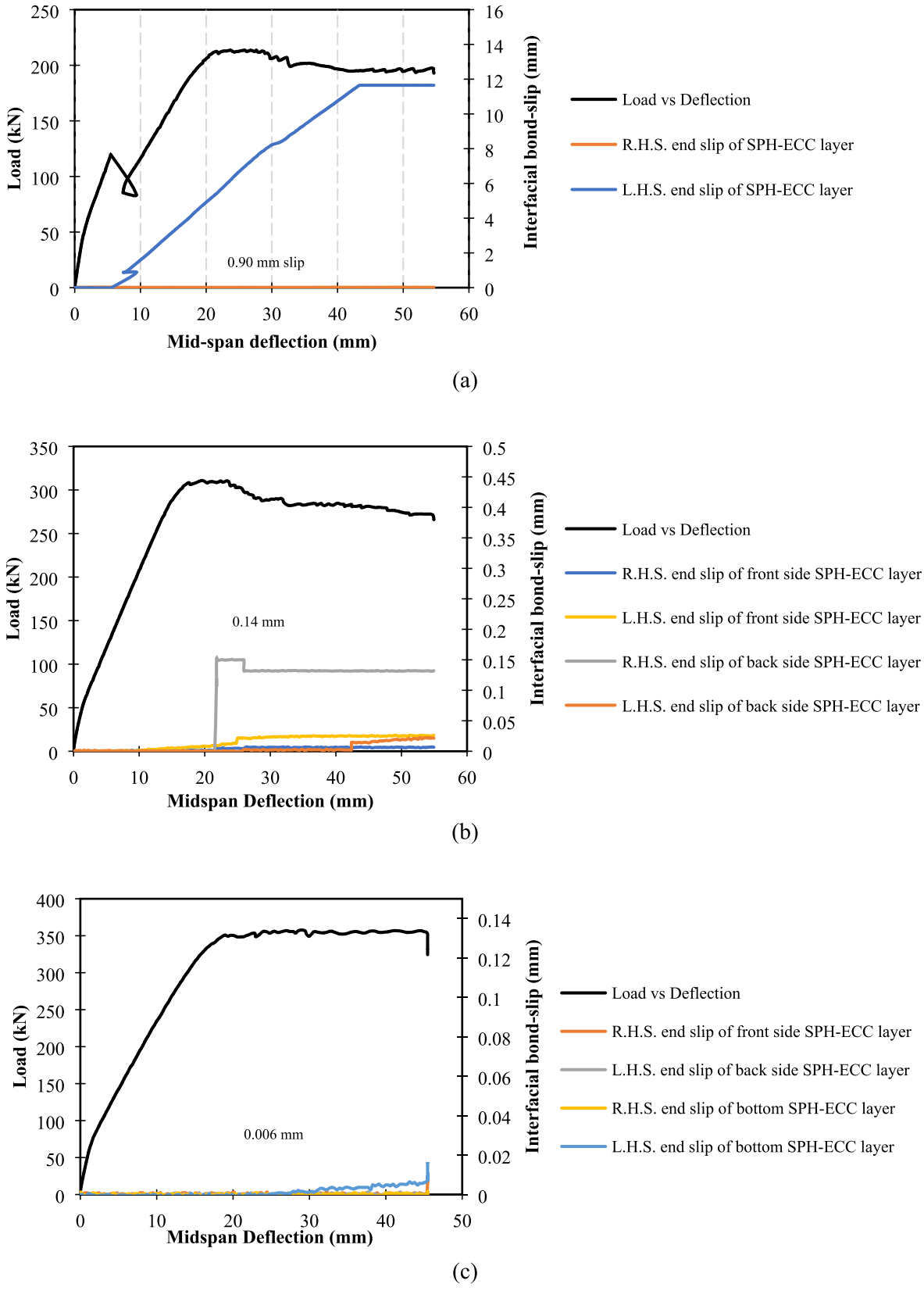

Fig. 11. Interfacial bond-slip recorded for the strengthened beams. (a) SB-1, (b) SB-2, (c) SB-3.

Table 4
Maximum interfacial bond end slips between SPH-ECC and RC beams.

Beam	Maximum slip (mm)
SB-1 (L.H.S. bottom SPH-ECC layer)	11.49
SB-2 (R.H.S. back side SPH-ECC layer)	0.14
SB-3(L.H.S. bottom SPH-ECC layer)	0.006

cameras while "back side" SPH-ECC layer refers to the layer at the opposite side of the beam. For SB-2, a small jump of interfacial bond-slip of 0.14 mm was recorded for the back side SPH-ECC layer in the RHS shear span just after concrete crushing occurred and after the peak load was reached. Fig. 11b also shows that other that this small bond-slip, negligible amounts of bond-slip were observed at all other sides and support ends. For SB-3, Fig. 11c clearly showed that virtually no bond-slip was occurred at all sides and supports ends even after concrete crushing at the top surface of the bending span until the end of test. A summary of the maximum recorded interfacial bond-slips recorded is given in Table 4.

Fig. 11 shows that the interfacial bond-slip behaviours were mainly affected by the strengthen configuration scheme used. The SB-1 which has the smallest contact area resulted showed the largest amount of bond-slip. The interfacial bond-slip also started well before the peak strength was reached. For SB-2, by applying the SPH-ECC layer at the two sides rather than at the RC beam soffit, the contact area between the SPH-ECC and concrete was increased and while the interfacial stress was reduced. As a result, only a small amount of bond-slip was recorded after the peak load was reached. For SB-3, it was found that the bottom SPH-ECC layer remained in full contact with the RC beam soffit even after the beam failure. It appears that the side SPH-ECC layers not only increased the contact area between the SPH-ECC and the RC beam part but also might have provided additional resistance to the bottom layer against debonding by reducing the shear stresses at the bottom interface.

3.3. Crack width analysis

DIC analysis was performed for all tests to record the cracking behaviour and crack propagation history of the beams. The accuracy of the DIC was first validated by comparing the midspan deflection curves obtained from DIC with those from LVDT which showed almost perfect agreements in Fig. 12. The cracking behaviours and patterns of the beams were then studied by analysing data retrieved from the DIC measurements.

For the CB, the first crack was observed in the pure bending span at a load of 27.4 kN at the end of the uncracked phase (Fig. 7). Subsequently, the number of cracks and crack width increased as the midspan deflection increased. These cracks also gradually propagated towards the top surface. At the end of the test, ten major cracks with width

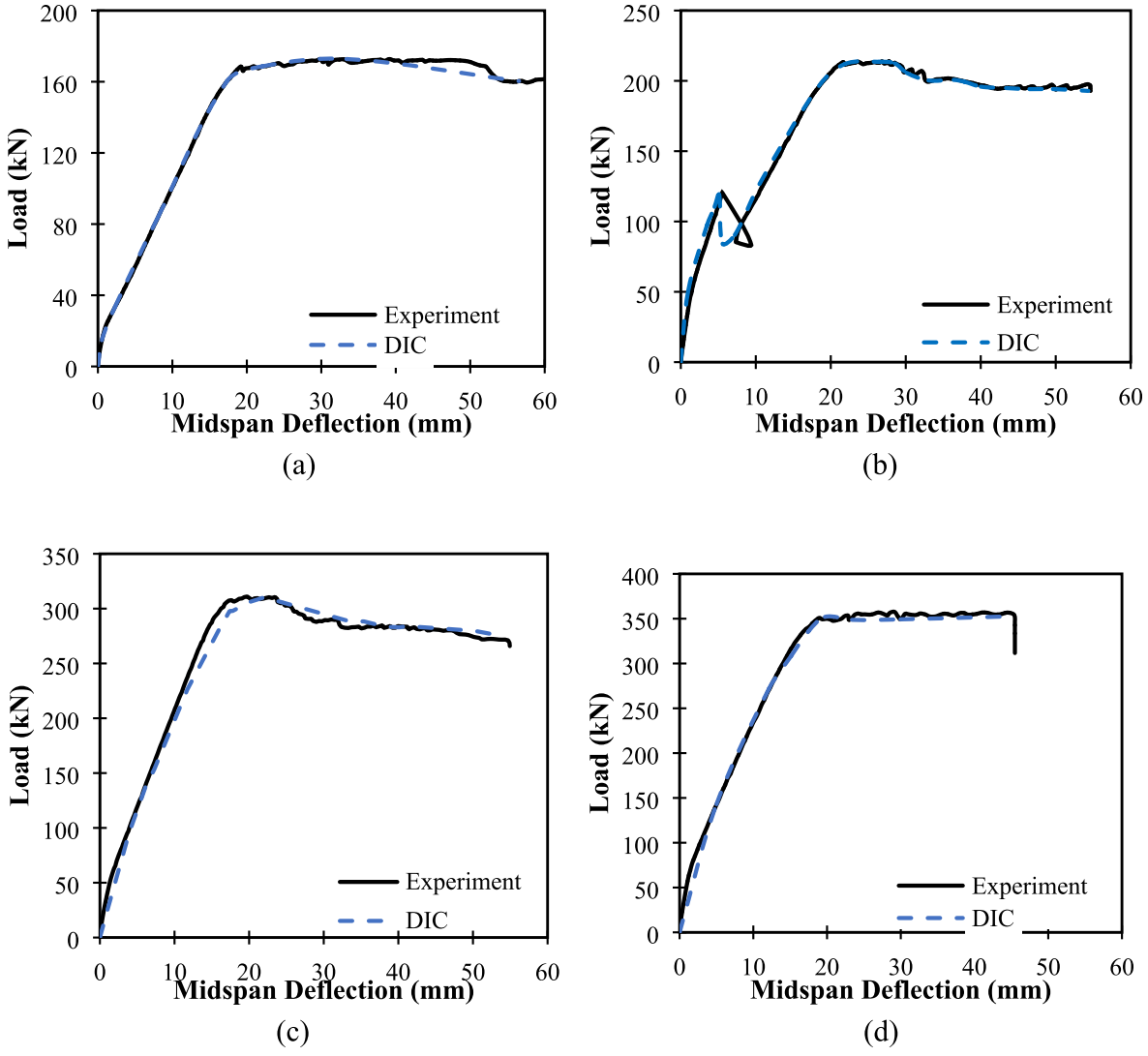

Fig. 12. Midspan-deflection curves comparison between LVDT and DIC measurements. (a) CB, (b) SB-1, (c) SB-2, (d) SB-3.

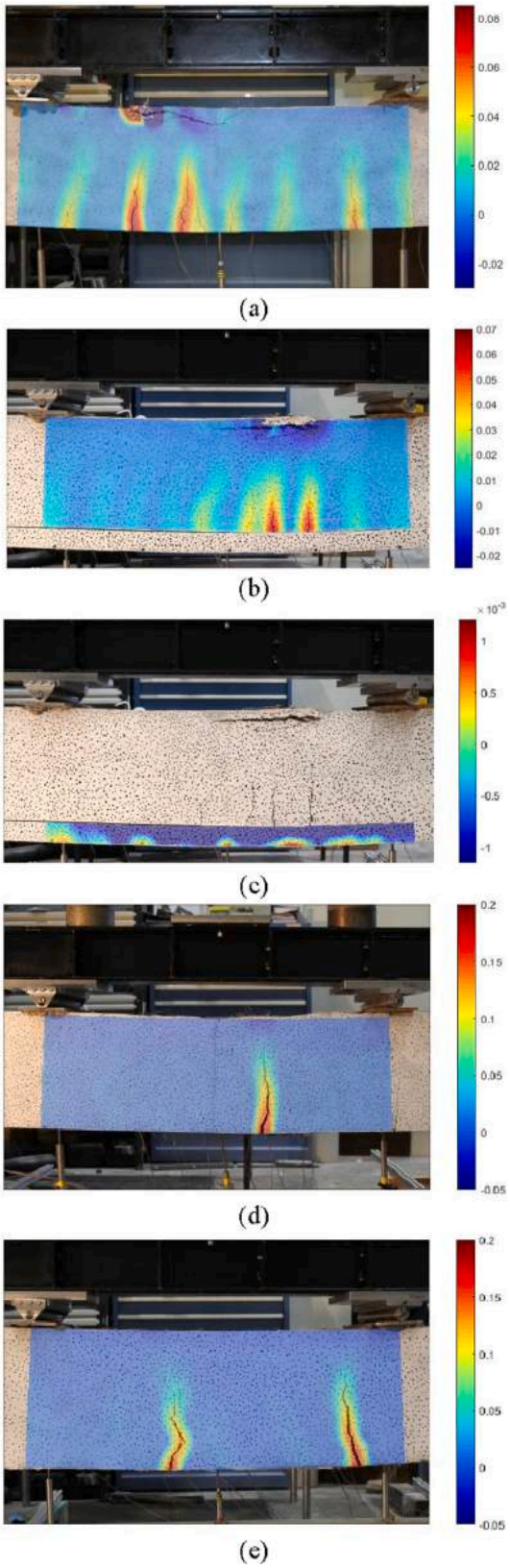

Fig. 13. Cracking pattern observed through DIC analysis after beam failure. (a) CB, (b) SB-1 RC beam part, (c) SB-1 bottom SPH-ECC layer, (d) SB-2, (e) SB-3.

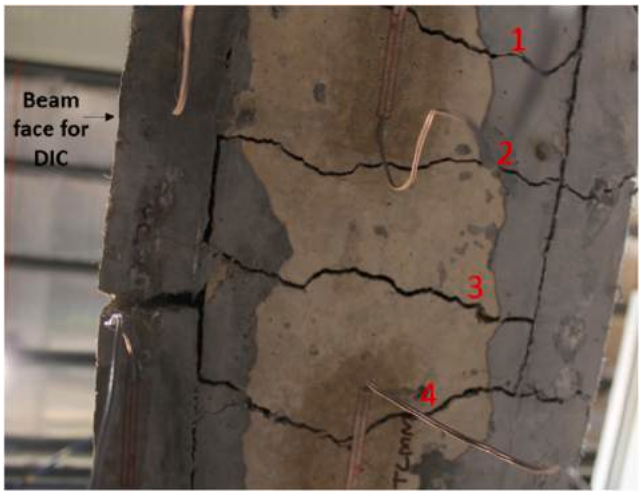

Fig. 14. Cracking pattern at SB-2 beam soffit at end of test.

ranging from 1.1 mm to 8.5 mm was observed. As shown in Fig. 13a, their depths were approximately 200 mm measuring from the beam soffit.

For SB-1, it was found that just after the interfacial debonding occurred when the loading was approximately 119 kN, fine cracks started to appear in the pure bending span of the RC beam part. After the concrete was crushed at top surface of the beam, ten major cracks were found within the pure bending span with widths ranging from 0.48 mm to 7.3 mm and depths up to 148 mm (Fig. 13b). However, no major crack was observed within the SPH-ECC layer throughout while test (Fig. 13c). It should be noted here that the cracking pattern, crack numbers and crack widths of the RC beam part of SB-1 were similar to that of CB. This was because after the premature interfacial debonding, the RC beam part and the SPH-ECC layer were bent independently.

For SB-2, the first crack was observed for the SPH-ECC layer when the loading was 110 kN. However, it is believed that cracks actually had formed in the RC beam part when the load was between 55 and 65 kN which led to the change of the slope of the load-deflection curve (Fig. 7). These cracks within the RC beam part were then propagated towards but restrained by the SPH-ECC layer. Since SPH-ECC has a much higher ductility and cracking strain than concrete, the appearance of cracks on the SPH-ECC surface was delayed unit a higher loading of 110kN. This cracking sequence was supported by the crack pattern observed at the beam soffit after the test (Fig. 14). From Fig. 14, it can be seen that four

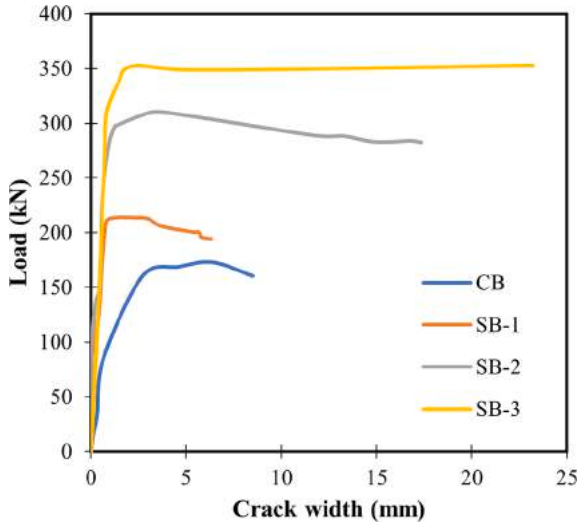

Fig. 15. Growth history of total crack width from DIC analysis.

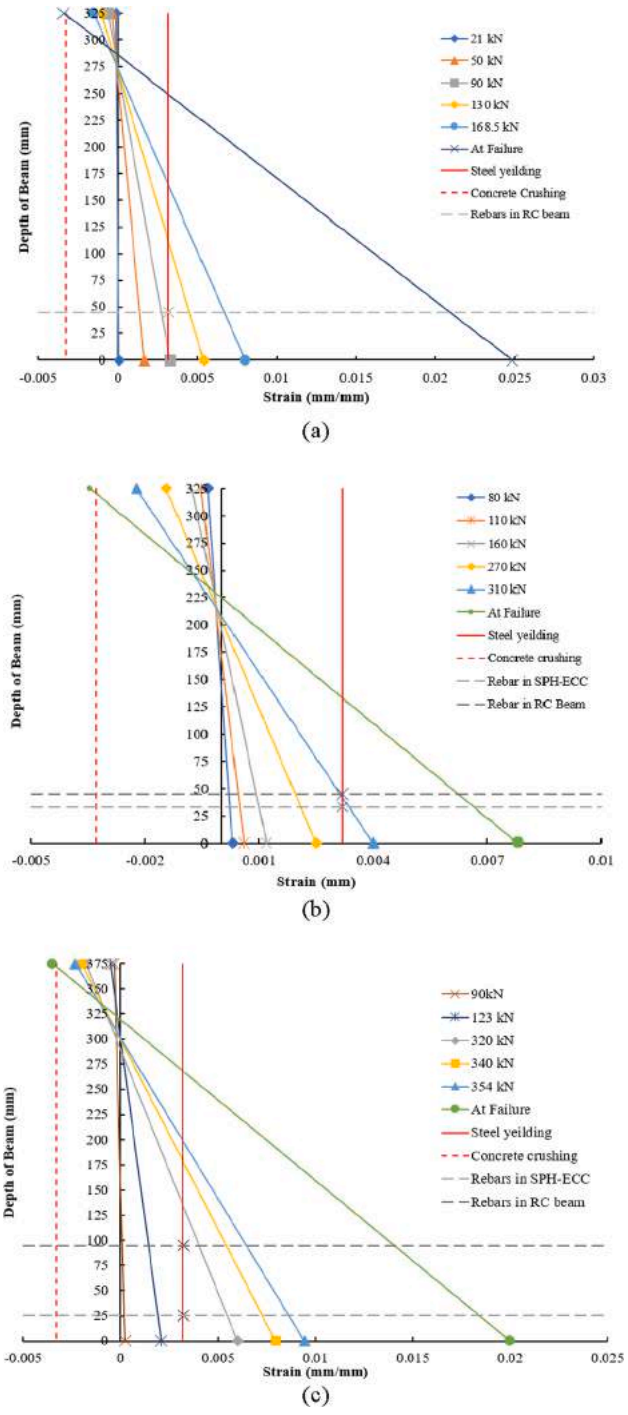

Fig. 16. Development of strain along beam depth at the beam mid-span. (a) CB, (b) SB-2, (c) SB-3.

major cracks were formed in the RC beam part. However, due to the restraint provided by side SPH-ECC layers, propagation of these four cracks were restrained at the SPH-ECC and concrete interface so that for the front side SPH-ECC layer only one major crack was formed until the end of the test. For the back side SPH-ECC layer, only two of these four cracks were propagated to the SPH-ECC layer. Detailed analysis of the DIC results shown that at the end of the test, for the front side SPH-ECC layer (Fig. 13d), eight minor cracks were developed at the beginning of the crack phase but only one of them was eventually developed to a major crack with a final width of 17.36 mm.

For SB-3, the first fine crack was observed in front side SPH-ECC

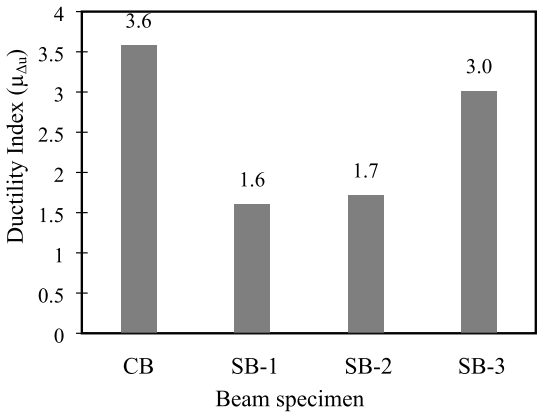

Fig. 17. Ductility Index of the tested beams.

layer when the load level was 123 kN. Since both the front and back side SPH-ECC layers were connected to through the bottom SPH-ECC layer, the crack restraining ability was more effective than SB-2. As a result, at the beginning of the crack phase, only four minor cracks were observed in the front side SPH-ECC layer. Out of these four cracks, one was eventually developed into a major crack (the RHS crack in Fig. 13e) when the peak load of 354 kN was reached at a midspan deflection of 20 mm. As the mid-span deflection increased to 32 mm, another minor crack (LHS crack in Fig. 13e) was also developed to a major crack.

Through detailed analysis of the DIC data, the growth histories of the total crack width (i.e. total width of all major cracks formed during the tests) for the tested beams are summarized in Fig. 15. It can be seen from Fig. 15 that the total crack width in CB started to increase well before that peak load (168.5 kN). However, for the strengthened beams, due to the presence of SPH-ECC layer(s) which restrained the crack growth rate, their total crack widths remained stable before the peak loads was reached and only increased substantially after the beams were failed.

3.4. Strain distributions

The development of strain distributions along the beam depth are plotted in Fig. 16 for the tested beams at different loading levels by using the best fitted data obtained from DIC and strain gauges. The strain distribution of SB-1 was not plotted because no further increase in tensile strain at the bottom surface of SPH-ECC layer was observed due to the premature interfacial debonding. The yield strain of reinforcement bar (0.31%) and peak compressive strain of concrete (0.33%) are also plotted as solid and dotted vertical lines in Fig. 16, respectively. The failure load in Fig. 16 refers to the load level when concrete crushing occurred. In general, from the DIC and strain gauges data obtained from SB-2 and SB-3, linear strain distribution was observed along the depth of the sections. Fig. 16a shows that the CB was under-reinforced and the reinforcement bars was yielded before 130 kN (77% of peak load 168.5 kN). For SB-2 (Fig. 16b), the reinforcement bars embedded in SPH-ECC layers were yielded just before the peak load (310 kN), while the reinforcement bars in RC beam part were yielded after the peak load. Fig. 16b indicates that soon after the yielding of reinforcement bars in the SPH-ECC layers and the RC beam part, the concrete was crushed at the top surface. Such a failure was rather close to a balanced failure which is expected as the two addition reinforcement bars were added to the beam (Fig. 1c) without increasing the overall depth of the beam. For SB-3, Fig. 16c shows that reinforcement bars in the SPH-ECC layer yielded at about 320kN (90% of the peak load 354kN). It should be noted here that even after reaching the peak load, concrete crushing was not occurred until a much larger deflection was achieved which indicated that the beam was still much under-reinforced. This was actually caused by the use of the U-shape encasement and the lower positions of the reinforcement bars inside the bottom SPH-ECC layer which

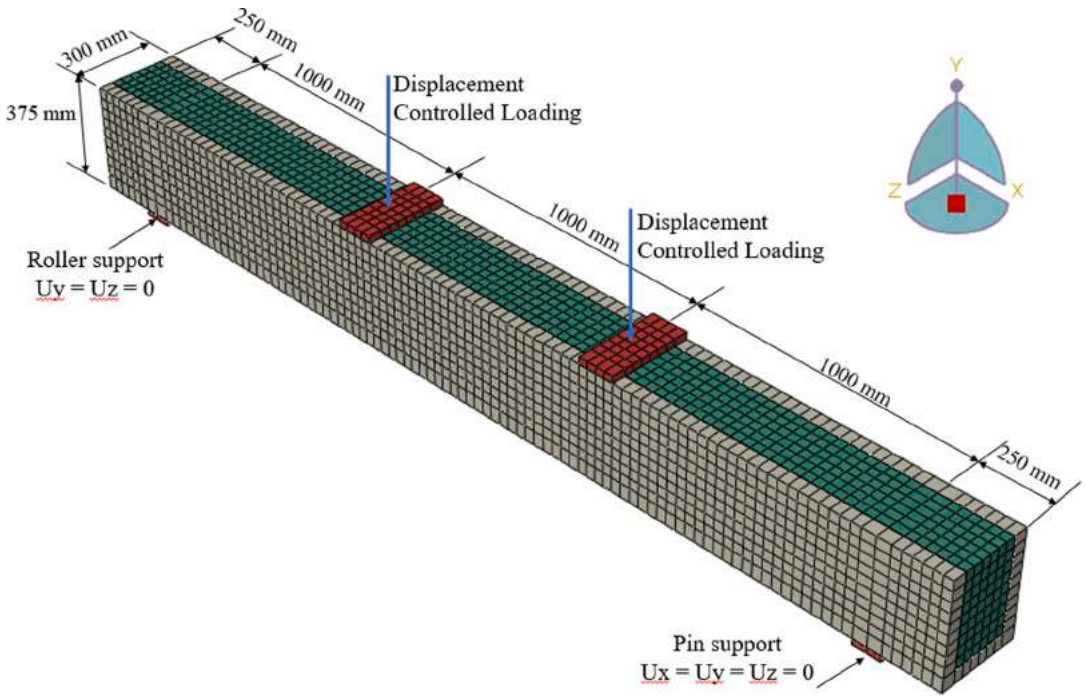

Fig. 18. A typical FE mesh (with 45 mm nominal element size) used for the modelling of the SB-3 beam.

increased the depth of the neutral axis of the beam cross-section.

3.5. Ductility index

In this study, ductility of the test beams is evaluated by using the ductility index $\mu_{\Delta u}$ which is calculated from load-midspan deflection curves using Eq. (1) [47].

$$\mu_{\Delta u} = \Delta_u / \Delta_y \quad (1)$$

In Eq. (1), Δ_u is the ultimate midspan deflection when concrete crushing occurred and Δ_y is the midspan-deflection at yielding of the reinforcement bars (in concrete for the CB and SB-1 and in SPH-ECC layers for SB-2 and SB-3). The ductility index obtained are summarized Fig. 17. As expected, since the CB was designed as an under-reinforced beam, it showed a high value of $\mu_{\Delta u} = 3.6$. For SB-1, due to premature interfacial bond-slip, the ductility index was reduced to 1.6. Similarly, as SB-2 was closed to a balance reinforced beam, its ductility index was reduced to 1.7 despite a higher peak load was achieved. However, for SB-3 while additional reinforcement bars were added and the peak load doubled, due to the U-shape SPH-ECC configuration and the increase in the section depth, the beam was still under-reinforced with only a small reduction of $\mu_{\Delta u}$ from 3.6 to 3.0. Thus, it can be concluded that U-shape strengthening configuration used in SB-3 could provide effective flexural strengthen enhancement while maintaining the beam's ductility.

4. Finite element analysis

In this study, three dimensional (3D) non-linear finite element (FE) models were developed for the implicit analysis of tested beams using the general purpose software ABAQUS [40]. Both material and geometric nonlinearities were considered. In order to capture the interfacial bond behaviour between SPH-ECC and concrete, a bond-slip model was also adopted. Both the loading and support boundary conditions were modelled as used in the actual tests.

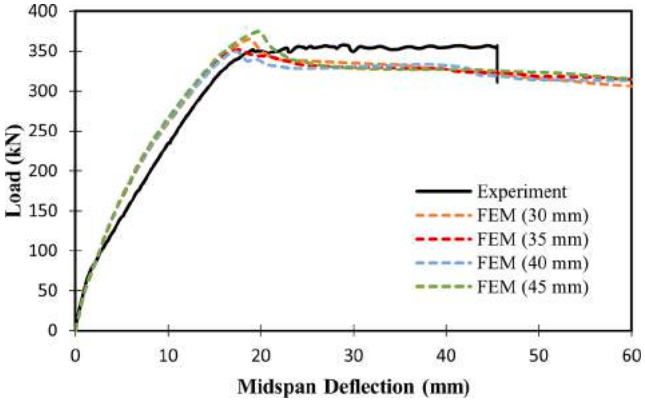

Fig. 19. Mesh sensitivity analysis for the SB-3 beam.

Table 5
Concrete Damage Plasticity (CDP) parameters for concrete and SPH-ECC.

ψ	∈	fb0/fc0	K_C	μ_V
36°	0.1	1.16	0.667	1.0E-4

4.1. Element used and element size sensitivity study

The eight-node solid brick element (C3D8R), which has been demonstrated to model the flexural behaviours of composite structures [48] accurately was employed to discretise the concrete and SPH-ECC parts. As no bond-slip between the reinforcement bars and concrete/ECC was observed in all tests, truss elements were used to model the reinforcement bars by using the embedded region constraint, which is also the most common and simplest method for reinforcement bar modelling [49]. Based on the previous study [48] with similar beam

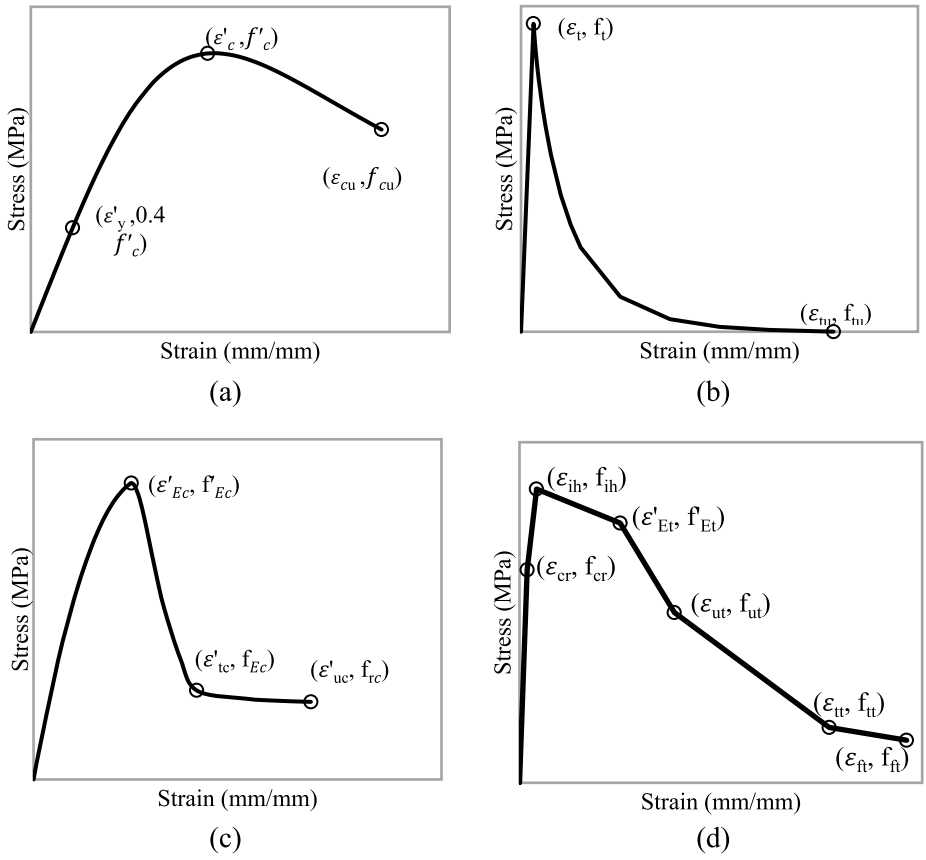

Fig. 20. Stress-strain relationship for concrete and SPH-ECC. (a) concrete under uniaxial compression, (b) concrete under uniaxial tension, (c) SPH-ECC under uniaxial compression, (d) SPH-ECC under uniaxial tension.

Table 6
Values of stress-strain parameters for concrete.

Compression				Tension			
Strain (%)		Stress (MPa)		Strain (%)		Stress (MPa)	
ε_c	0.1	0.4f'$_c$	12.0	ε_t	0.01	f_t	3.0
ε_o	0.33	f'$_c$	30.0	ε_{tu}	0.25	f_{tu}	0.0
ε_{ou}	0.7	f_{cu}	24.4	–	–	–	–

specimen dimensions, an element size sensitivity study with four different nominal element sizes ranging from 30 mm to 45 mm (along the longitudinal direction of the beam) was performed and a typical FE mesh for SB-3 is shown in Fig. 18. The element size sensitivity results (Fig. 19) shows that a nominal element size of 35 mm could produce results with good accuracy. Thus, models with a 35 mm nominal element size were selected for the analyses of all tested beams.

4.2. Material models

The concrete damage plasticity (CDP) model in ABAQUS was selected to define the behaviours of concrete and SPH-ECC as it was able to simulate the tensile and compressive behaviours of concrete and SPH-ECC accurately [21,48]. Table 5 shows the key parameters for the CDP model used which were based on the values used in previous successful studies [21,48,50,51].

In order to predict the responses of the tested beams accurately, the use of the correct concrete material model is essential. The constituent model proposed by Carriera and Chu [52] was employed to describe the behaviour of concrete under compression (Eq. (2)). Values of the key parameters (Fig. 20a) of this model were taken from the actual material tests of the concrete used and are listed in Table 6. The tensile behaviour of concrete was defined by the constitutive model proposed by Hassan [53] (Eq. (3)) and values of the key parameters were also determined by actual material tests (Table 6).

$$f_c = f'_c \left[\frac{\beta\left(\frac{\varepsilon}{\varepsilon'_c}\right)}{\beta - 1 + \left(\frac{\varepsilon}{\varepsilon'_c}\right)^{\beta}} \right] \tag{2a}$$

$$\beta = \left| \frac{f'_c}{32.4} \right|^3 + 1.55 \tag{2b}$$

$$f_t = \begin{cases} \varepsilon E_c & 0 < \varepsilon \le \varepsilon'_{tc} \\ f'_{tc} exp\left[-\left(\frac{\varepsilon - \varepsilon'_{tc}}{\alpha_1} \right)^{\beta_1} \right] & \varepsilon'_{tc} < \varepsilon \le \varepsilon_{tu} \end{cases} \tag{3a}$$

$$\varepsilon_{tu} = 25\varepsilon'_{tc}, \quad \alpha_1 = 0.00035, \quad \beta_1 = 0.85 \tag{3b}$$

In Eq. (2), f'_c is the peak compressive stress in MPa while ε'_c is the corresponding strain obtained. In Eq. (3), f'_{tc} is the peak tensile stress of concrete in MPa, obtained through indirect tensile tests. $\varepsilon'_{tc} = f'_{tc}/E_c$ is the corresponding strain of f'_{tc}. E_c is the elastic modulus of concrete in MPa.

For SPH-ECC, the material properties in compression (Eqs. (4) to (6) and Fig. 20c) were defined by using the constitutive model proposed by Khan et al. [43].

Table 7
Values of stress-strain parameters for SPH-ECC under compression.

Specimen	ε'_{Ec}	f'_{Ec}	ε'_{tc}	f_{Ec}	ε'_{uc}	F_{rc}
SB-1	0.54	65.0	0.81	32.5	2.7	20.3
SB-2	0.56	70.0	0.84	35.0	2.8	20.9
SB-3	0.59	75.0	0.89	37.5	2.9	21.6

Note: Strain in percentage, stress in MPa.

Fig. 21. Uniaxial tensile test of SPH-ECC dog-bone specimen.

$$f_{Ec} = \begin{cases} f'_{Ec}\left[\dfrac{\varepsilon}{\varepsilon'_{Ec}}\{0.8\left(1-\dfrac{\varepsilon}{\varepsilon'_{Ec}}\right)+1\right] & 0 \le \varepsilon \le \varepsilon'_{Ec} \\ f'_{Ec}\left[\dfrac{n(\varepsilon/\varepsilon'_{Ec})}{1+(n-2)\left(\dfrac{\varepsilon}{\varepsilon'_{Ec}}\right)+(\varepsilon/\varepsilon'_{Ec})^2}\right]+f'_{rc} & \varepsilon'_{Ec} < \varepsilon \le \varepsilon'_{uc} \end{cases} \quad (4)$$

In Eq. (4), f'_{Ec} is the peak compressive stress of SPH-ECC in MPa and ε'_{Ec} is the corresponding strain. ε'_{uc} is the ultimate compressive strain. n is the controlling parameter of curve shape during post peak softening so that

$$n = -f'_{rc}\left[\frac{\varepsilon'^{2}_{Ec} - 2\varepsilon'_{Ec}\varepsilon'_{tc} + \varepsilon'^{2}_{tc}}{\varepsilon'_{Ec}\varepsilon'_{tc}(f'_{rc} - f'_{Ec})}\right] \quad (5)$$

In Eq. (5), ε'_{tc} is the transition point for strain in the post peak region. f'_{rc} is the residual strength in MPa and is given by

$$f'_{rc} = f'_{Ec}(3.1(f'_{Ec})^{-0.55}) \quad (6)$$

The values of the key parameters using in Eq. (4), Eq. (5) and Eq. (6) for different batches of SPH-ECC used in the fabrication of the strengthened beams (SB-1, SB-2 and SB-3) were obtained from the average test results of standard cylinder tests and are listed in Table 7.

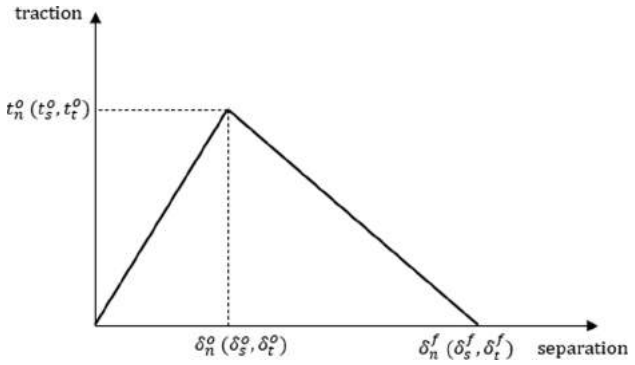

Fig. 22. Traction separation model used in interfacial bond-slip modelling.

For SPH-ECC under tension, the multi-linear model proposed by Khan et al. [54] (Eq. (7) and Fig. 20d) is employed to define the stress-strain relationship.

$$f_{Et} = \begin{cases} \dfrac{f_{cr}}{\varepsilon_{cr}}\varepsilon & 0 \le \varepsilon \le \varepsilon_{cr} \\ f_{cr} + (f_{ih} - f_{cr})\left(\dfrac{\varepsilon - \varepsilon_{cr}}{\varepsilon_{ih} - \varepsilon_{cr}}\right) & \varepsilon_{cr} \le \varepsilon \le \varepsilon_{ih} \\ f_{ih} + (f'_{Et} - f_{ih})\left(\dfrac{\varepsilon - \varepsilon_{ih}}{\varepsilon'_{Et} - \varepsilon_{ih}}\right) & \varepsilon_{ih} \le \varepsilon \le \varepsilon'_{Et} \\ f'_{Et} + (f_{ut} - f'_{Et})\left(\dfrac{\varepsilon - \varepsilon'_{Et}}{\varepsilon_{ut} - \varepsilon'_{Et}}\right) & \varepsilon'_{Et} \le \varepsilon \le \varepsilon_{ut} \\ f_{ut} + (f_{tt} - f_{ut})\left(\dfrac{\varepsilon - \varepsilon_{ut}}{\varepsilon_{tt} - \varepsilon_{ut}}\right) & \varepsilon_{ut} \le \varepsilon \le \varepsilon_{tt} \\ f_{tt} + (f_{ft} - f_{tt})\left(\dfrac{\varepsilon - \varepsilon_{tt}}{\varepsilon_{ft} - \varepsilon_{tt}}\right) & \varepsilon_{tt} \le \varepsilon \le \varepsilon_{ft} \end{cases} \quad (7)$$

In Eq. (7), f_{cr} and ε_{cr} are the first cracking stress (MPa) and corresponding strain, respectively. f_{ih} and ε_{ih} are the peak tensile stress (MPa) and corresponding strain, respectively. f'_{Et} and ε'_{Et} are the tensile stress (MPa) and strain at the point where the SPH-ECC tensile strength start to drop significantly with a very steep slope accompanied with crack localization (i.e., formation of major cracks). f_{ut} (MPa) and ε_{ut} are the ultimate limit point of stress-strain curve. f_{tt}(MPa) and ε_{tt} represents the point where softening transition phase starts to be stabilized. Lastly, f_{ft} (MPa) and ε_{ft} define the failure point. The values of the key parameters used in Eq. (7) for different batches of SPH-ECC used in the fabrication of the strengthened beams (SB-1, SB-2 and SB-3) were obtained from the lower bound test results of dog-bone tensile tests (Fig. 21) and are listed in Table 8.

4.3. Interfacial bond-slip modelling

As interfacial bond-slip was observed in SB-1 and SB-2, it is essential to include a proper bond-slip model in the FE model. In this study, surface-to-surface contact elements based on the traction-separation constitutive model [40,55] were inserted between all SPH-ECC and concrete interfaces to model the interfacial bond-slip and cohesive behaviours. This model consists of a linear elastic response up to the damage initiation. After reaching the damage initiation criteria, the

Table 8
Values of stress–strain parameters for SPH-ECC under tension.

Specimen	ε_{cr}	f_{cr}	ε_{ih}	f_{ih}	ε'_{Et}	f'_{Et}	ε_{ut}	f_{ut}	ε_{tt}	f_{tt}	ε_{ft}	f_{ft}
SB-1	0.04	4.0	0.07	4.3	0.45	4.0	0.93	2.8	1.5	2.1	2.5	1.0
SB-2	0.01	5.7	0.06	6.7	0.4	6.4	0.58	5.0	1.0	3.0	2.5	1.5
SB-3	0.05	5.0	0.11	6.9	0.65	6.5	1.0	4.0	2.0	1.3	2.5	1.0

Note: Strain in percentage and stress in MPa.

Table 9
Value of parameters for interface modelling.

Friction Coefficient, μ	K_n, K_s, K_t (N/mm^3)	Damage		
		$\delta_n^o, \delta_s^o, \delta_t^o$ (mm)	$\delta_m^{max} - \delta_m^o$ (mm)	Viscosity Coefficient
0.7	40	0.03	0.001	0.001

Table 10
Comparisons of peak loads.

Specimen	Load carrying capacity		
	$P_{peak\text{-}Test}$ (kN)	$P_{peak\text{-}FEM}$ (kN)	$P_{peak\text{-}FEM}$/ $P_{peak\text{-}Test}$
CB	168.5	169.5	1.00
SB-1	213.4	222.0	1.04
SB-2	310.0	307.1	0.99
SB-3	354.0	351.7	0.99

damage evolution of interfacial bond will be continued until the complete bond failure (Fig. 22). The linear elastic traction-separation response can be defined as

$$\begin{Bmatrix} t_n \\ t_s \\ t_t \end{Bmatrix} = \begin{bmatrix} K_n & 0 & 0 \\ 0 & K_s & 0 \\ 0 & 0 & K_t \end{bmatrix} \begin{Bmatrix} \delta_n \\ \delta_s \\ \delta_t \end{Bmatrix} \tag{8}$$

In Eq. (8), K_n, K_s, and K_t are stiffnesses across the interface. t_n, t_s and t_t represent nominal traction with corresponding the separations δ_n, δ_s and δ_t, respectively. Subscripts *n, s*, and *t* denotes the normal, first and second shear directions respectively. As the tractions increase, eventually when the quadratic-separation based damage criterion shown in Eq. (9) is satisfied, the damage of interfacial bond will be initiated.

$$\left\{\frac{\langle \delta_n \rangle}{\delta_n^o}\right\}^2 + \left\{\frac{\delta_s}{\delta_s^o}\right\}^2 + \left\{\frac{\delta_t}{\delta_t^o}\right\}^2 = 1 \tag{9}$$

In Eq. (9), $\langle . \rangle$ denotes the Macaulay bracket to signify that pure compressive displacement that does not initiate damage. δ_n^o, δ_s^o, and δ_t^o are respectively peak values of separation during linear elastic response in normal, shear, and tangential directions. After the damage initiation, it will be followed by damage softening response. The damage softening response under combined normal, shear, and tangential separations is defined through an effective separation term δ_m such that

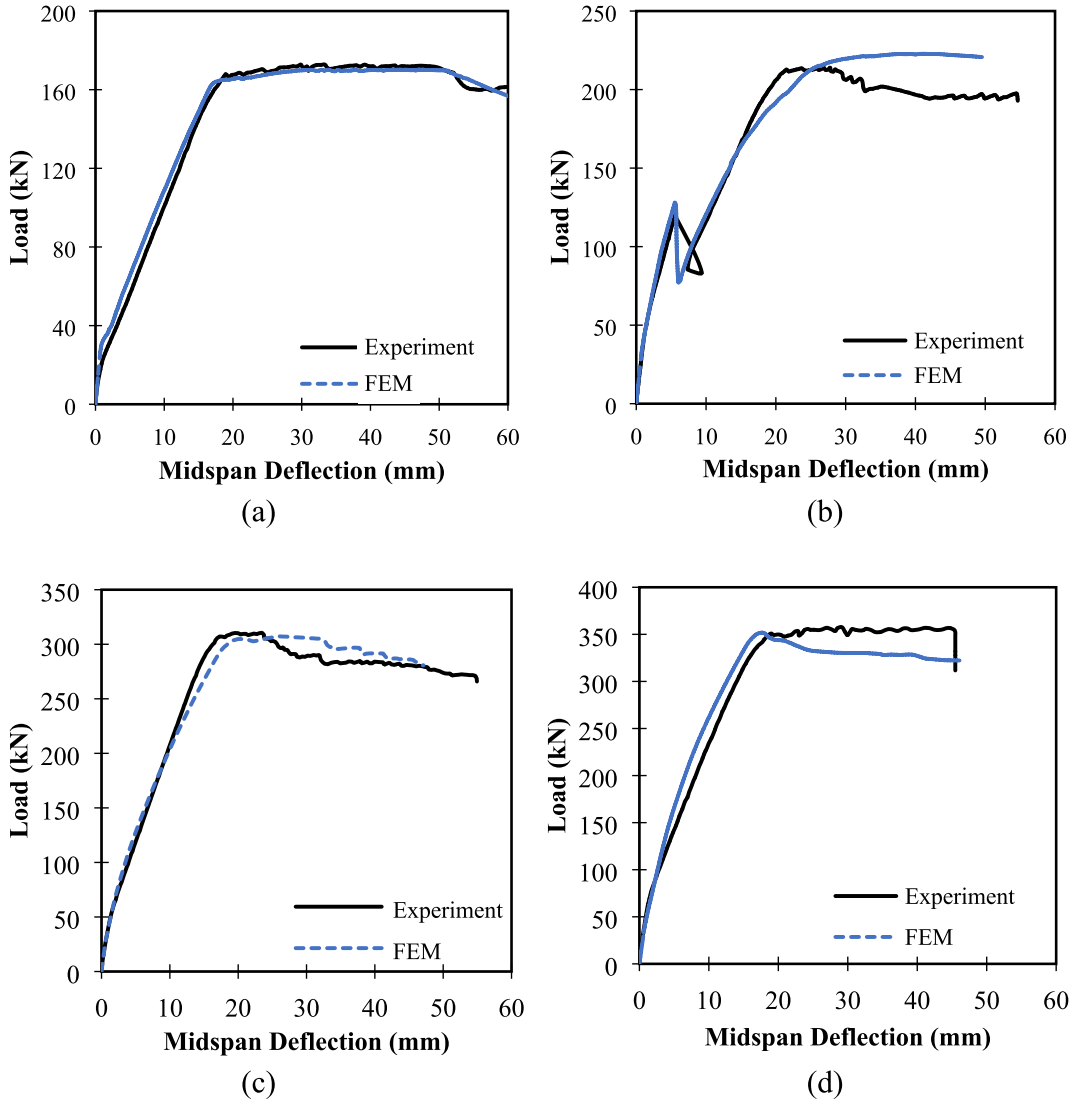

Fig. 23. Comparison of load-deflection curves. (a) CB, (b) SB-1, (c) SB-2, (d) SB-3.

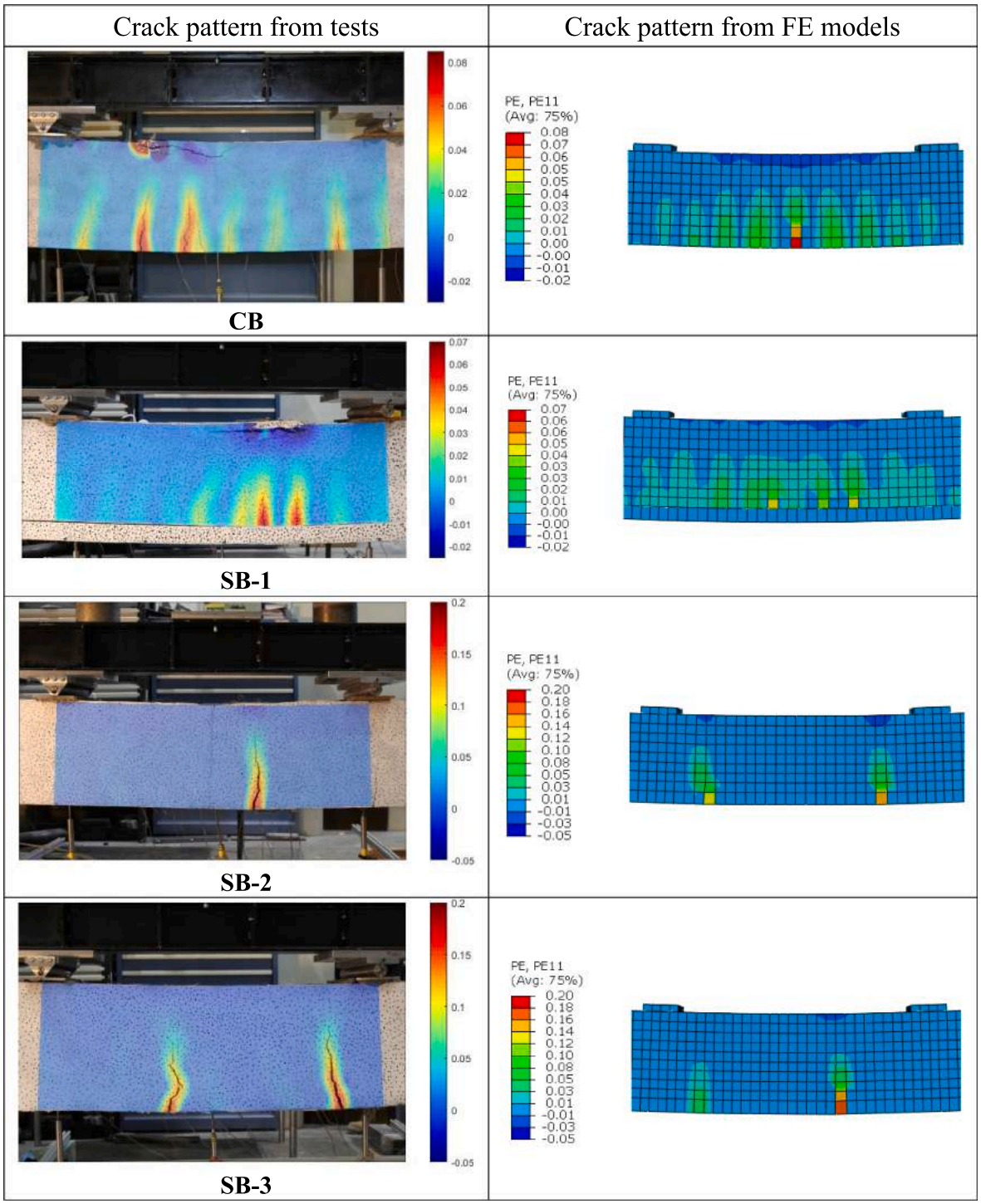

Fig. 24. Comparison of cracking patterns of tested beams at failure.

$$\delta_m = \sqrt{\langle \delta_n \rangle^2 + {\delta_s}^2 + {\delta_t}^2} \tag{10}$$

so that the following linear-softening damage variable D can be defined.

$$D = \frac{\delta_m^f(\delta_m^{max} - \delta_m^o)}{\delta_m^{max}(\delta_m^f - \delta_m^o)} \tag{11}$$

In Eq. (11), δ_m^o, and δ_m^f are the effective separations at damage initiation and complete failure, respectively. δ_m^{max} is the maximum value of effective separation attained during the loading history.

The damage initiation, evolution and stabilization parameters employed to define interfacial bond behaviour between concrete and SPH-ECC are listed in Table 9. Their values were obtained by calibrating the FE modelling results of the strengthened beams with the experimental results using the method proposed by Valikhani et al. [56]. Note that such an approach for obtaining interfacial parameters has shown to be reliable for predicting the interface bond-slip between concrete and ultra-high performance concrete (UHPC) with fibres. Since the UHPC materials modelled by Valikhani et al. [56] was a fibre-based material and ECC is also a fibre-based materials, they show similar interface behaviours with concrete. Therefore, it is reasonable to adopt Valikhani

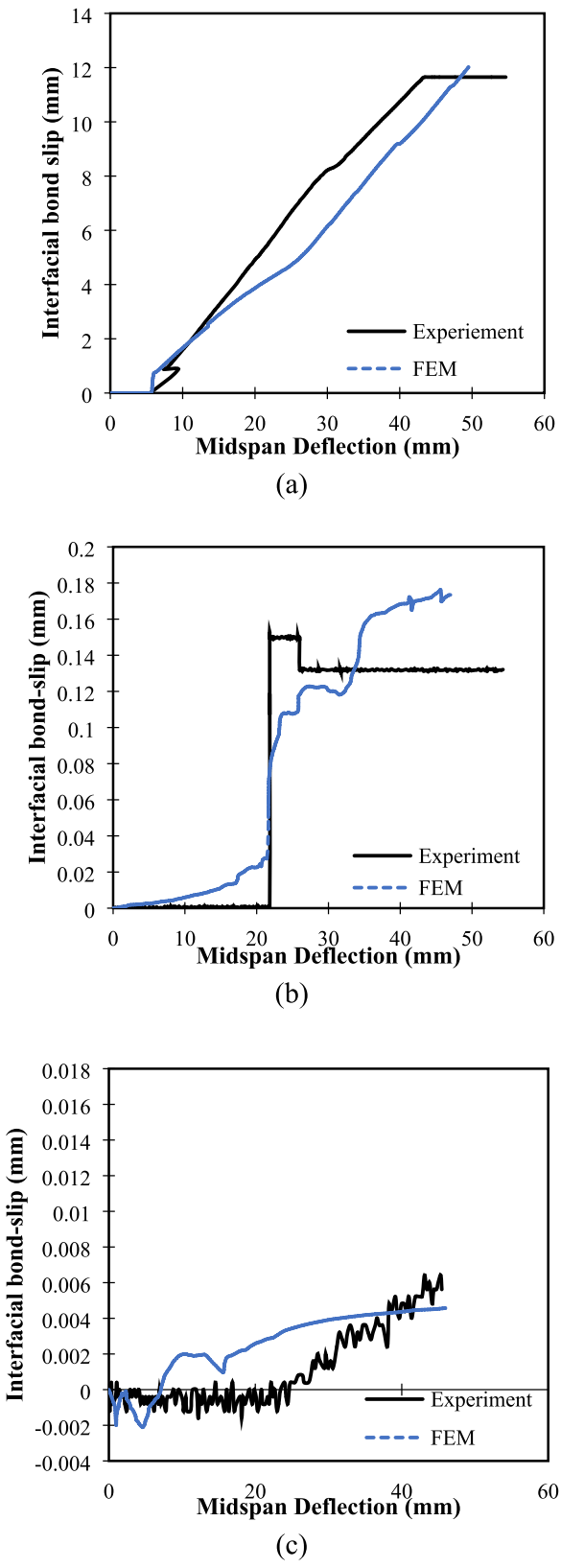

Fig. 25. Comparison of interfacial bond-slip. (a) SB-1, (b) SB-2, (c) SB-3.

et al.'s [56] method to obtain values of parameters here for concrete and SPH-ECC interface. Since it was observed in the SB-1 test that debonding failure was sudden and brittle, a difference of 0.001 mm between the effective separation at damage initiation (δ_m^o) and the maximum value of effective separation (δ_m^{max}) was used. In Table 9, the viscosity coefficient used will control the damage stability. In order to reflect the brittle bond-slip between SPH-ECC and concrete, a low value of 0.001 was set as the viscosity coefficient to represent rapid energy release.

4.4. FE model validation

Comparisons of the predicted peak loads ($P_{peak\text{-}FEM}$) obtained from FE models with the peak loads from tests ($P_{peak\text{-}Test}$) for all beams are presented in Table 10. The complete predicted load-deflection curves are also compared with the test curves in Fig. 23. It can be seen form Table 10 that the peak loads obtained from the FE models agreed well with the test results. In addition, Fig. 23 shows that the FE models could also capture the three distinctive phases (Section 3.1) observed during the beam tests with good agreements. Furthermore, the proposed modelling approach could also predict the sudden load drop due to the premature debonding in SB-1 (Fig. 23b). The damage patterns of the modelled beams at failure are compared with those observed from tests in Fig. 24. From Fig. 24, it can be seen that good agreements were obtained for all tested beams.

The proposed FE models were further validated by comparing predicted interfacial bond-slips with those observed in tests for the strengthened beams (Fig. 25). Fig. 25 shows that while the bond-slip behaviour could be affected by the random surface roughness of the interface during casing, reasonably good agreements were obtained between the modelling results and the actual measurements. Therefore, the proposed FE models in this study could be used in future research to conduct a parametric study which is critical for the development of analytical models to predict the flexural behaviours of the strengthened beams and for practical design calculations.

5. Conclusion

In this study, flexural strengthening of reinforced concrete (RC) beam using steel and polyvinyl-alcohol engineered cementitious composite (SPH-ECC) with embedded steel reinforcement bars was investigated. Three different strengthening configurations in which the SPH-ECC layer was only applied at the soffit of the RC beam part (SB-1), at the two sides of the RC beam part (SB-2) and at both sides together at the soffit of the RC beam part (SB-3) were suggested. Together with the control RC beam (CB), the three strengthened beams were tested under four-point bending until failure. The flexural performance of strengthened beams was compared in terms of peak load, failure mode, load-midspan deflection curve, cracking pattern, interfacial bond-slip between SPH-ECC and concrete, strain distribution and ductility. To complement the experimental study, a finite element (FE) modelling approach using surface-to-surface cohesive model was also proposed to predict the flexural behaviours of the strengthened beams including the interfacial bond-slip between the RC beam part and the SPH-ECC strengthening layers. Based on the experimental and numerical modelling results, the following conclusions can be drawn.

1. Premature failure due to significant interfacial debonding was observed in SB-1. For SB-2 and SB-3, their final flexural failures were caused by concrete crushing at the top surface within the pure bending span. For SB-2, shortly after the concrete crushing, a small amount of interfacial bond-slip was observed. On the other hand, for SB-3, virtually no interfacial bond-slip was observed even after concrete crushing was occurred.
2. For the cracking pattern at failure, it was found that the cracking pattern of SB-1 was similar to that of the CB. For SB-1, due to premature interfacial bond-slip, no major cracking was appeared in the SPH-ECC layer even after the beam failed. For SB-2 and SB-3, it was observed that cracks were initiated from the RC beam part and propagated towards SPH-ECC layers. It was found that SPH-ECC demonstrated a good crack width control ability and those cracks

originated from the RC beam part were restrained by the SPH-ECC layers effectively.

3. The load carrying capacity of strengthened beam was found to be highly sensitive to the strengthening configuration. While SB-2 only showed a small increase of 26.6% when compared with the CB, SB-2 and SB-3 increased the peak strength by 185% and 210%, respectively. The ineffectiveness of SB-1 was due to the premature bond-slip between the RC beam part and the SPH-ECC layer. While both SB-2 and SB-3 greatly enhanced the flexural strength, SB-3 showed a higher enhancement than SB-2. This was because the U-shape encasement used in SB-2 not only generated a larger and deeper beam section (thus low the neutral axis), it also reduced interfacial bond stress by providing a larger contact surface area between the SPH-ECC layers and the RC beam parts. In addition, the U-shape encasement also provided a more effective restraint that prevented those cracks originated from the RC beam part from propagating to the SPH-ECC layers.
4. Comparison of proposed FE modelling and experimental results showed that good predictions were obtained for the load-midspan deflection curves, cracking patterns, interfacial bond-slip behaviours as well as the final failure modes of the strengthened beams. Hence, the proposed model could be used in the future to conduct a parametric study to allow engineers and designers to gain a more insight on the flexural behaviours of the strengthened beams.

CRediT authorship contribution statement

M. Qasim: Methodology, Investigation, Software, Writing – original draft. **C.K. Lee:** Conceptualization, Methodology, Supervision, Resources, Writing – review & editing. **Y.X. Zhang:** Supervision, Writing – review & editing.

Declaration of Competing Interest

The authors declare that they have no known competing financial interests or personal relationships that could have appeared to influence the work reported in this paper.

Data availability

All data were presented in the paper.

Acknowledgment

UNSW Canberra's support for this research through Tuition Fee Scholarship is gratefully acknowledged. The authors appreciate the UNSW Canberra's TSG staff for their valuable support in the experimental challenges.

References

[1] Teng JG, Chen JF, Smith ST, Lam L. FRP Strengthened RC Structures. West Sussex. UK: John Wiley and Sons Ltd; 2002.
[2] Chen Y, Davalos J, Ray I, Kim HY. Accelerated aging tests for evaluations of durability performance of FRP reinforcing bars for concrete structures. Compos Struct 2007;78(1):101–11.
[3] Abdalla JA, Harib F, Hawileh R, Mirghani A. Experimental investigation of bond slip behavior of almunium plates adhesively bonded to concrete. J Adhes Sci Technol 2016;30(25):82–99.
[4] Vandoros KG, Dritsos SE. Concrete jacket construction detail effectiveness when strengthening RC coulumns. Constr Build Mater 2008;22(3):264–76.
[5] Chang SY, Chen TW, Tran NC, Liao WI. Seismic retrofitting of RC columns with RC jackets and wing walls with different structural details. Earthq Eng Eng Vib 2014;13:279–92.
[6] Shehata IAE, Shehata LCD, Santos EWF, Simões MLF. Strengthening of reinforced concrete beams in flexure by partial jacketing. Mater Struct 2009;42:495–504.
[7] Alhadid MMA, Youssef MA. Analysis of reinforced concrete beams strengthened using concrete jackets. Eng Struct 2017;132:172–87.
[8] Ruano G, Isla F, Pedraza RI, Sfer D, Luccioni B. Shear retrofitting of reinforced concrete beams with steel fiber reinforced concrete. Constr Build Mater 2014;54:646–58.
[9] Jongvivatsakul P, Bui LVH, Koyekaewphring T, Kunawisarut A, Hemstapat N, Stitmannaithum B. Using Steel Fiber-Reinforced Concrete Precast Panels for Strengthening in Shear of Beams: An Experimental and Analytical Investigation. Adv Civil Eng 2019;2019:4098505.
[10] Tanarslan HM, Alver N, Jahangiri R, Yalçınkaya Ç, Yazıcı H. Flexural strengthening of RC beams using UHPFRC laminates: Bonding techniques and rebar addition. Constr Build Mater 2017;155:45–55.
[11] Lampropoulos AP, Paschalis SA, Tsioulou OT, Dritsos SE. Strengthening of reinforced concrete beams using ultra high performance fibre reinforced concrete (UHPFRC). Eng Struct 2016;106:370–84.
[12] Nagaprasad P, Sahoo DR, Rai DC. Seismic strenghthening of RC columns using external steel cage. Earthq Eng Struct Dyn 2010;38(14):1563–86.
[13] Aykac S, Kalkan I, Aykac B, Ozbek E. Strengthening of RC T-beams with perforated steel plates. Mag Concr Res 2012;65(1):37–51.
[14] Adhikary BB, Mutsuyoshi H. Shear strengthening of RC beams with web-bonded continuous steel plates. Constr Build Mater 2006;20(5):296–307.
[15] Sharif A, Al-Sulaimani GJ, Basunbul IA, Baluch MH, Husain M. Strengthening of shear-damaged RC beams by external bonding of steel plates. Mag Concr Res 1995;47(173):329–34.
[16] Ye LP, Yue QR, Zhao SH, Li QW. Shear strength of reinforced concrete columns strengthened with carbon fiber reinforced plastic sheet. J Struct Eng 2003;128(12):1527–34.
[17] Tanarslan HM. Repairing and strengthening of earthquake-damaged RC beams with CFRP strips. Mag Concr Res 2010;62(5):365–78.
[18] Zhang W, Kanakubo T. Flexural strengthening of RC beams with externally bonded CFRP plate: experimental study on shear-peeling debonding. Mag Concr Res 2016;68(14):724–38.
[19] Julio ENBS, Branco FAB, Silva VD. Concrete-to-concrete bond strength. Influence of the roughness of the substrate surface. Constr Build Mater 2004;18(9):675–81.
[20] Deng M, Zhang Y, Li Q. Shear strengthening of RC short columns with ECC jacket: Cyclic behavior tests. Eng Struct 2018;160:535–45.
[21] Al-Osta MA, Isa MN, Baluch MH, Rahman MK. Flexural behavior of reinforced concrete beams strenghtened with ultra-high performance fiber reinforced concrete. Constr Build Mater 2017;134:279–96.
[22] Yuan F, Chen M, Pan J. Flexural strengthening of reinforced concrete beams with high-strength steel wire and engineered cementitious composites. Constr Build Mater 2020;254:119284.
[23] Zheng YZ, Wang WW, Brigham JC. Flexural behaviour of reinforced concrete beams strengthened with a composite reinforcement layer: BFRP grid and ECC. Constr Build Mater 2016;115:424–37.
[24] Kim YY, Lee BY, Bang JW, Han BC, Feo L, Cho CG. Flexural Peroformance of reinforced concrete bemas strengthend with strain-hardening cementitious composite and high strength reinforcing steel bar. Compos B 2014;56:512–9.
[25] Yang X, Gao WY, Dai JG, Lu ZD, Yu KQ. Flexural strengthening of RC beams with CFRP grid-reinforced ECC matrix. Compos Struct 2018;189:9–26.
[26] Hung CC, Chen YS. Innovative ECC jacketing for retrofitting shear-deficient RC memebrs. Constr Build Mater 2016;111:408–18.
[27] Shang XY, Yu JT, Li LZ, Lu ZD. Strengthening of RC Structures by Using Engineered Cementitious Composites: A Review. Sustainability 2019;11(12):3384.
[28] Krishnaraja AR, Kandasamy S. Flexural Performance of Hybrid Engineered Cementitious Composite Layered Reinforced Concrete Beams. Periodica Polytechnica. Civ Eng 2018;11748.
[29] Pourfalah S. Behaviour of engineered cementitious composites and hybrid engineered cementitious composites at high temperatures. Constr Build Mater 2018;158:921–37.
[30] Zhang J, Wang Q, Wang Z. Properties of Polyvinyl Alcohol-Steel Hybird Fiber-Reinforced Composite with High-Strength Cement Matrix. J Mater Civ Eng 2017;29:04017026.
[31] Qasim M, Lee CK, Zhang YX. An experimental study on interfacial bond strength between hybrid engineered cementitious composite and concrete. Constr Build Mater 2022;356:129299.
[32] Rawat S, Lee CK, Zhang YX. Performance of fibre-reinforced cementitious composites at elevated temperatures: A review. Constr Build Mater 2021;292:123382.
[33] Ahmed SFU, Mihashi H. Corrosion durability of strain hardening fiber reinforced cementitious composites. Aust J Civ Eng 2010;8(1):13–26.
[34] Tinoco MP, Silva FA. Repair of pre-damaged RC beams using hybrid fiber reinforced strain hardening cementitious composites. Eng Struct 2021;235:112081.
[35] Lu C, Leung CKY. Theoretical evaluation of fiber orientation and its effects on mechanical properties in Engineered Cementitious Composites (ECC) with various thickness. Cem Concr Res 2017;95:240–6.
[36] Tayeh BA, Bakar BHA, Johari MAM, Voo YL. Mechanical and permeability properties of the interface between normal concrete substrate and ultra high performance fiber concrete overlay. Constr Build Mater 2012;36:538–48.
[37] Yıldırım G, S¸ahmaran M, Al-Emam MKM, Hameed RKH, Al-Najjar Y, Lachemi M. Effects of Compressive Strength, Autogenous Shrinkage, and Testing Methods on Bond Behavior of High-EarlyStrength Engineered Cementitious Composites. ACI Mater J 2015;112(3):409–18.
[38] Zanotti C, Banthia N, Plizzari G. A study of some factors affecting bond in cementitious fiber reinforced repairs. Cem Concr Res 2014;63:117–26.
[39] Zanotti C, Rostagno G, Tingley B. Further evidence of interfacial adhesive bond strength enhancement through fiber reinforcement in repairs. Constr Build Mater 2018;160:775–85.

[40] Abaqus/CAE User's Manual; 2014.
[41] ASTM A370-21. Standard Test Methods and Definitions for Mechanical Testing of Steel Products; 2021.
[42] Meng D, Haung T, Zhang YX, Lee CK. Mechanical behaviour of a polyvinyl alcohol fibre reinforced engineered cementitious composite (PVA-ECC) using local ingredients. Constr Build Mater 2017;141:259–70.
[43] Khan MKI, Zhang YX, Lee CK. Mechanical properties of high-strength steel-polyvinyl alcohol hybrid fibre engineered cementitious composites. J Struct Integrity Maint 2021;6(1):47–57.
[44] Product Data Sheets: AVDA 650 New generation PCE-based high range water reducer; GCP. Applied Technologies, Australia.
[45] AS 1478.1-2000. Chemical admixtures for concrete, mortar and grout Part 1: Admixtures for concrete; 2000.
[46] Wu C, Li VC. CFRP-ECC hybrid for strengthening of the concrete structures. Compos Struct 2017;178:372–82.
[47] Qin F, Zhang Z, Yin Z, Di J, Xu L, Xu X. Use of high strength, high ductility engineered cementitious composites (ECC) to enhance the flexural performance of reinforced concrete beams. J Build Eng 2020;32:101746.
[48] Kabir MI, Lee CK, Rana MM, Zhang YX. Flexural and bond-slip behaviours of engineered cementitious composites encased steel composite beams. J Constr Steel Res 2019;157:229–44.
[49] Khalil AEH, Etman E, Atta A, Essam M. Nonlinear behavior of RC beams strengthened with strain hardening cementitious composites subjected to monotonic and cyclic loads. Alex Eng J 2016;55(2):1483–96.
[50] Bahraq AA, Al-Osta MA, Khan MI, Ahmad S. Numerical and analytical modelling of seismic behavior of beam-column joints retrofitted with ultra-high performance fiber reinforced concrete. Structures 2021;32:1986–2003.
[51] Al-Huri MA, Al-Osta MA, Ahmad S. Finite Element Modelling of Corrosion-Damaged RC beams Strengthened Using the UHPC Layers. Materials 2022:15.
[52] Carreira D, Chu K. Stress-strain relationship for plain concrete in compression. ACI J 1985:797–804.
[53] Hassan MK. Behaviour of Hybrid Stainless-Carbon Steel Composite Beam-Column Joints. Australia: Western Sydney University; 2016. PhD. Thesis.
[54] Khan MKI, Lee CK, Zhang YX. Parametric study on high strength ECC-CES composite column under axial compression. J Build Eng 2021;44:102883.
[55] Khan MKI, Lee CK, Zhang YX. Numerical modelling of engineered cementitious composits-concrete encased steel composite columns. J Constr Steel Res 2020;170:106082.
[56] Valikhani A, Jahromi AJ, Mantawy IM, Azizinamini A. Numerical Modelling of Concrete-to-UHPC Bond Strength. Materials 2020;13:1379.